

The matter fluctuation amplitude inferred from the weak lensing power spectrum and correlation function in CFHTLenS data

Tianhuan Lu ¹★ and Zoltán Haiman ¹

¹*Department of Astronomy, Columbia University, New York, NY 10027, USA*

13 May 2020

ABSTRACT

Based on the cosmic shear data from the Canada-France-Hawaii Telescope Lensing Survey (CFHTLenS), Kilbinger et al. (2013) obtained a constraint on the amplitude of matter fluctuations of $\sigma_8(\Omega_m/0.27)^{0.6} = 0.79 \pm 0.03$ from the two-point correlation function (2PCF). This is $\approx 3\sigma$ lower than the value 0.89 ± 0.01 derived from *Planck* data on cosmic microwave background (CMB) anisotropies. On the other hand, based on the same CFHTLenS data, but using the power spectrum, and performing a different analysis, Liu et al. (2015) obtained the higher value of $\sigma_8(\Omega_m/0.27)^{0.64} = 0.87^{+0.05}_{-0.06}$. We here investigate the origin of this difference, by performing a fair side-by-side comparison of the 2PCF and power spectrum analyses on CFHTLenS data. We find that these two statistics indeed deliver different results, even when applied to the same data in an otherwise identical procedure. We identify excess power in the data on small scales ($\ell > 5,000$) driving the larger values inferred from the power spectrum. We speculate on the possible origin of this excess small-scale power. More generally, our results highlight the utility of analysing the 2PCF and the power spectrum in tandem, to discover (and to help control) systematic errors.

Key words: gravitational lensing: weak – cosmology: observations – cosmology: theory – large-scale structure of Universe

1 INTRODUCTION

Weak gravitational lensing (WL) is a promising probe of the mass distribution in the Universe, via observations of correlated distortions in the shapes of background galaxies (e.g. Bartelmann & Schneider 2001; Refregier 2003; Hoekstra & Jain 2008; Kilbinger 2015). Weak lensing has also matured as a method to measure the parameters of the background Λ cold dark matter (Λ CDM) cosmological model. Several recent WL surveys have yielded competitive constraints on cosmological parameters, including the Canada-France-Hawaii Telescope Lensing Survey (CFHTLenS; Heymans et al. 2012; Kilbinger et al. 2013), the Kilo-Degree Survey (KiDS; Kuijken et al. 2015; Hildebrandt et al. 2016; Köhlinger et al. 2017), the Dark Energy Survey (DES; Abbott et al. 2016; Troxel et al. 2018), and the Subaru Hyper Suprime-Cam (HSC; Aihara et al. 2017b,a; Hikage et al. 2019) survey.

As the size and depth of weak lensing surveys have increased, a moderate tension has emerged on parameter constraints, especially on the matter density fluctuation ampli-

tude σ_8 , between the results from weak lensing and from the cosmic microwave background (CMB). Specifically, Planck 2018 (Aghanim et al. 2018), based on the CMB, inferred the joint constraint on σ_8 and the matter density Ω_m , $\Sigma_8 \equiv \sigma_8(\Omega_m/0.3)^\alpha = 0.83 \pm 0.01$ for $\alpha = 0.5$ (or equivalently $\sigma_8(\Omega_m/0.27)^{0.6} = 0.89 \pm 0.01$). Kilbinger et al. (2013), based on WL data in CFHTLenS, found $\sigma_8(\Omega_m/0.27)^{0.6} = 0.79 \pm 0.03$, which is lower than the Planck value by $\sim 3\sigma$ (note: all error-bars correspond to 68% confidence). Similar discrepancies have been identified between other WL surveys (e.g. Hildebrandt et al. 2016; Köhlinger et al. 2017; Hikage et al. 2019), and Planck’s earlier results (Ade et al. 2016).

An exception to this trend is the analysis of the CFHTLenS lensing data by Liu et al. (2015, hereafter L15), who have found a higher fluctuation amplitude, close to the Planck value. L15 performed a set of N -body simulations on a grid of 91 cosmological models with a range of Ω_m , σ_8 , and w values (where w is the equation of state parameter for dark energy), and replicated the sky positions, redshifts, and shape noise of ~ 4 million galaxies from the public CFHTLenS data. They fit the simulations to the observed data using two different statistics: the convergence power spectrum, and the abundance of lensing peaks

★ E-mail: tl2854@columbia.edu

(defined as local maxima on the convergence maps). They inferred $\sigma_8(\Omega_m/0.27)^{0.64} = 0.87^{+0.05}_{-0.06}$ and $0.84^{+0.04}_{-0.03}$, respectively, from these statistics.

These results are especially interesting, because Kilbinger et al. (2013) and L15 are based on the same WL survey and use a similar pipeline for parameter estimation, but their constraints differ at the 2σ significance. We also note that Kilbinger et al. (2013) used a different statistic – the two-point correlation function (2PCF) of the WL shear – which could cause a discrepancy. These two statistics have yielded different values in the KiDS data, with Hildebrandt et al. (2016) finding $\sigma_8(\Omega_m/0.3)^{0.5} = 0.745 \pm 0.039$ using the 2PCF, and Köhlinger et al. (2017) finding the lower value $\sigma_8(\Omega_m/0.3)^{0.5} = 0.651 \pm 0.058$ using the power spectrum.

In this paper, we focus on the difference between power spectrum and 2PCF, and explore the reasons for the discrepancy on Σ_8 between L15 and other weak lensing works, primarily Kilbinger et al. (2013). In § 2 we summarise salient features of the CFHTLenS data, and how we processed them. In § 3, we describe our methodology, including the suite of ray-tracing simulations, and the likelihood analysis using the two different statistics. In § 4, we present our results, which reproduce the previous discrepancy, and then test possible reasons for this discrepancy. We then discuss our results, and several other possible data-related and physical explanations in § 5. Finally, we summarise our conclusions in § 6.

2 LENSING DATA

2.1 CFHTLenS shear catalogue

The CFHTLenS data covers four separate patches on the sky, W1→W4, consisting of 179 pointings in total, and covering a total survey area of 154 deg^2 . The CFHTLenS Catalogue, which includes specifications of all objects identified in their data, is publicly available (Erben et al. 2013). In this work, we use the galaxy shear data from the Catalogue, which was constructed with a pipeline consisting of several steps: (1) extract a galaxy catalogue by SExtractor (Bertin & Arnouts 1996), (2) estimate photometric redshifts with a Bayesian photo- z code (Benitez 2000), and (3) measure galaxy ellipticity values $\{e_1, e_2\}$, including multiplicative (m) and additive (c_2) bias corrections calibrated with *lensfit* (Miller et al. 2013).

Following L15, we filter the shear catalogue and keep only galaxies in the redshift range $0.2 \leq z \leq 1.3$ and weight $w > 0$ (the latter is assigned to each galaxy by *lensfit*, based on the significance of its ellipticity measurement), leaving ~ 4.2 million galaxies. We then project and rearrange the survey area into 13 square subfields with a size of 12 deg^2 each, for further map generation.

In order to mitigate the impact of systematic errors, Heymans et al. (2012) computed a systematics test parameter U for each pointing, and performed a selection based on this parameter. As a result of this procedure, 129 unique pointings are marked as having passed the systematics selection, effectively keeping $\sim 75\%$ of the data (~ 3.2 million galaxies). We include this selection for our results in § 4, and discuss its impact in § 5.1.

2.2 Convergence maps

In this section, we describe our steps to prepare convergence maps, on which the power spectrum calculations are performed. The lensing convergence (κ) represents a distance-weighted projection of the over-density along the line of sight. It cannot be measured from galaxy shapes directly, but it can be inferred from the lensing shear γ (Kaiser & Squires 1993), which, in turn, can be estimated from a smoothed galaxy ellipticity field, using the weak lensing approximation.

2.2.1 Identifying low galaxy number density regions

Due to bright stars and bad pixels, some part of the survey area is unusable for measuring galaxy shapes. These regions can be found in the CFHTLenS Catalogue by checking the local galaxy number density. Following L15, we identify these low number density regions by a criterion of $n_{\text{gal}} < 5 \text{ arcmin}^{-2}$ over a smoothing scale of 1 arcmin. Liu et al. (2014) found that the magnification bias introduced by such a selection process is negligible for CFHTLenS. Among the 13 square subfields, this criterion gives a good separation between normal and low-density regions, with average number densities of $n_{\text{normal}} = 9.1 \text{ arcmin}^{-2}$ and $n_{\text{low}} = 0.7 \text{ arcmin}^{-2}$ respectively.

2.2.2 Creating shear maps

In creating shear maps, normal and low-density regions contribute differently, so they are represented separately. In the normal-density regions, individual galaxies contribute in a discrete manner. Because galaxies have four properties, we define four fields as follows to characterize them:

$$\mathcal{X}(\boldsymbol{\theta}) = \sum_g^N \delta(\boldsymbol{\theta} - \boldsymbol{\theta}_g) \mathcal{X}_g, \quad (1)$$

$$\mathcal{X} \text{ is one of } \{\mathbf{e}, \mathbf{c}, m, w\} \quad (2)$$

where $\delta(\cdot)$ is the Dirac delta function, $g = 1 \rightarrow N$ the indices of individual galaxies, \mathbf{e}_g the two-component ellipticity, m_g and $\mathbf{c}_g = \{0, c_2\}$ the multiplicative and additive biases, w_g the weight. Note that \mathcal{X}_g in eq. (1) represents one of the dimensionless quantities of an individual galaxy, whereas $\mathcal{X}(\boldsymbol{\theta})$ represents a field with a dimension of $(\text{solid angle})^{-1}$, inheriting the dimension of the Dirac delta function.

In the low-density regions, we ignore the contribution from the galaxies and use zero shear with average weight density in a continuous manner as follows,

$$w_{\text{low}}(\boldsymbol{\theta}) = \begin{cases} \langle w \rangle \cdot n_{\text{normal}}, & \text{in normal-density regions} \\ 0, & \text{in low-density regions} \end{cases}, \quad (3)$$

where $\langle w \rangle$ is the average weight of the galaxies and $n_{\text{normal}} = 9.1 \text{ arcmin}^{-2}$ is the overall number density of galaxies in normal-density regions. This method is based on the assumption that the low-density regions have similar densities of galaxies as in normal regions but they are not observed, and their expected ellipticity is zero.

We calculate shear maps by applying a Gaussian

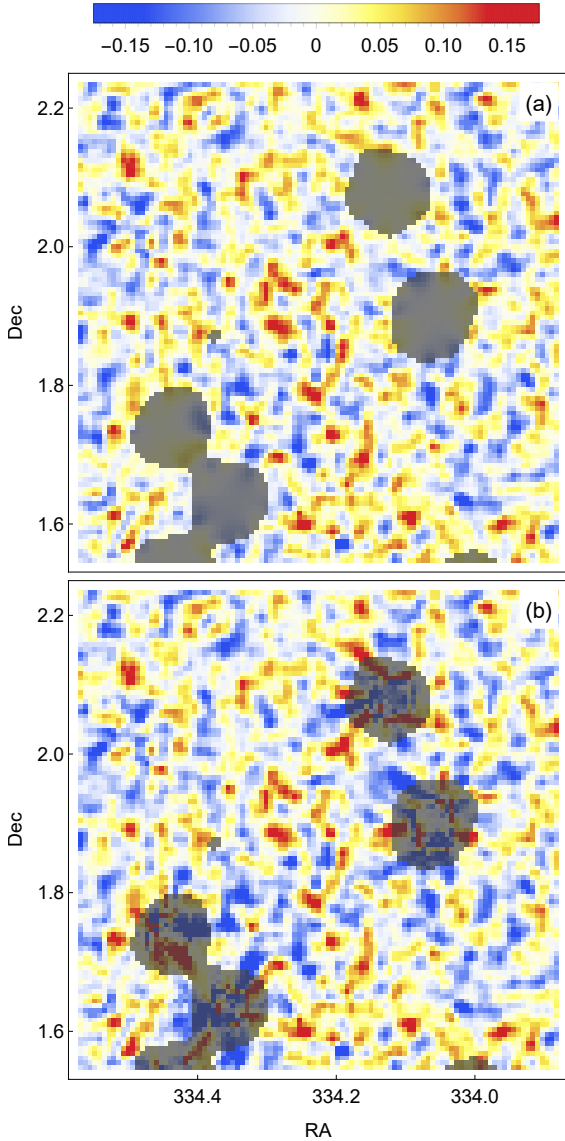


Figure 1. Example portions of convergence maps generated (a) in this work and (b) by the method in L15. Regions of low galaxy number density are marked by darker colours. Ignoring the weights of unobserved galaxies from low-density regions during the smoothing (see eq.(4)) causes exceptionally large fluctuations near the boundaries on the scale of $1 \sim 10$ pixels.

smoothing to the galaxy ellipticity fields with respect to the weight fields:

$$\gamma(\theta) = \int \frac{W_G(\theta - \theta')w(\theta')[\mathbf{e}(\theta') - \mathbf{c}(\theta')]}{W_G(\theta - \theta')\{w(\theta')[1 + m(\theta')] + w_{\text{low}}(\theta')\}} d\theta', \quad (4)$$

where we use a Gaussian kernel of scale $\theta_G = 0.5$ arcmin

$$W_G(\theta) = \frac{1}{2\pi\theta_G^2} \exp\left(-\frac{|\theta|^2}{2\theta_G^2}\right). \quad (5)$$

In L15, the smoothing process was the same except they did not consider the contribution from low density regions (effectively used $w_{\text{low}}(\theta) = 0$). We noticed that doing so lets the shear estimation in low-density regions be dominated by the shape noise from very few galaxies. As shown in Figure 1,

setting $w_{\text{low}}(\theta) = 0$ leads to high-frequency components near the boundary, because of the abrupt changes in the number density. This difference between L15 and our work significantly affects the power spectrum on small scales (we discuss the statistical impact of this effect in more detail in § 3.1.2 below).

2.2.3 Creating convergence maps

The lensing field can be expressed in terms of the lensing convergence κ and the complex-valued lensing shear $\gamma = \gamma_1 + i\gamma_2$. These two fields are related to the lensing potential field ψ by

$$\kappa(\theta) = \frac{1}{2} \nabla^2 \psi(\theta), \quad (6)$$

$$\gamma_1(\theta) = \frac{1}{2} (\psi_{,11} - \psi_{,22}), \quad (7)$$

$$\gamma_2(\theta) = \psi_{,12}, \quad (8)$$

where

$$\psi_{,ij} \equiv \frac{d^2\psi}{d\theta_i d\theta_j}. \quad (9)$$

Following Kaiser & Squires (1993), the convergence field is related to the shear field in Fourier space by

$$\hat{\kappa}(\ell) = \frac{(\ell_1^2 - \ell_2^2)\hat{\gamma}_1(\ell) + 2\ell_1\ell_2\hat{\gamma}_2(\ell)}{\ell_1^2 + \ell_2^2}, \quad (10)$$

where $\hat{\kappa}(\ell)$ and $\hat{\gamma}_{1,2}(\ell)$ denote the Fourier transform of $\kappa(\theta)$ and $\gamma_{1,2}(\theta)$ respectively. The Fourier transform and its inverse are performed on a 512×512 grid for each 12 deg^2 square subfield. The pixel size ~ 0.4 arcmin corresponds to a multipole of $\ell \sim 53,000$. A small portion of the convergence maps created in this work is shown in panel (a) in Figure 1 for illustration.

2.3 Mock catalogues and maps

In this work, we use the same mock galaxy shear catalogues as L15. We here briefly introduce the steps of generating these mock catalogues, and refer the reader to L15 for more details.

L15 picked 91 sampling points in a three-dimensional cosmological parameter space: $0 < \Omega_m < 1$, $-3 < w < 0$, and $0.1 < \sigma_8 < 1.5$, where the Latin hypercube sampling (McKay et al. 1979) was used to make the points statistically evenly distributed. They ran one N -body simulation at each point using a modified version of the Gadget-2 code (Springel 2005). N -body simulations were performed with 512^3 dark matter particles in boxes of size $(240h^{-1}\text{Mpc})^3$ starting from redshift $z = 100$, with the additional cosmological parameters set to constant values of $h = 0.72$ (Hubble constant), $\Omega_b h^2 = 0.0227$ (baryon density), and $n_s = 0.96$ (spectral index of scalar perturbations).

L15 used ray-tracing to create mock galaxy shears. At the sky position of each galaxy in the CFHTLenS Catalogue, they followed a light ray from redshift zero to the estimated galaxy redshift, and calculated its lensing shear based on the gravitational potential. The N -body simulation box for each cosmological model was randomly shifted and rotated to create 1,000 pseudo-independent random realizations.

Note that this procedure places galaxies at their observed locations, uncorrelated with the simulated field. In reality, the galaxies will reside in dark matter halos which are correlated with the nearby density field, introducing possible biases. However, we expect these biases to be negligible at the sensitivity of CFHT, given that the density field at the source plane is only weakly correlated with structures at the much lower-redshift peak of the lensing kernel (see Liu et al. (2014) for related discussion).

The lensing shear $\boldsymbol{\gamma}$ in the mock catalogue so far contains no noise. Following L15, we rotate the ellipticity of each individual galaxy in the real CFHTLenS Catalogue by a random angle, and take this to be the intrinsic ellipticity of that galaxy. This is justified by the fact that the r.m.s. cosmic shear signal contributes only of order 1% of the observed total ellipticity. We finally obtain the ellipticity in the mock catalogue, using the weak lensing approximation, as

$$\boldsymbol{\gamma}_{\text{mock}} = \mathbf{e}_{\text{mock}} = (1 + m)(\boldsymbol{\gamma} + \mathcal{R}(\varphi)\mathbf{e}), \quad (11)$$

where \mathbf{e} and m are the ellipticity and multiplicative correction of the real galaxy, \mathcal{R} a 2-dimensional rotation matrix, and φ a random number drawn from a uniform distribution $\mathcal{U}(-\pi, \pi)$.

After generating the mock shear catalogues, we apply the same method as described in § 2.2.3 for the real data, to generate mock convergence maps. These shear catalogues and convergence maps are then used to compute correlation functions and power spectra, as we describe in the next section.

3 METHODS

3.1 Statistics

We compare two statistics: the 2PCF of the shear, and the power spectrum of the convergence field. We compute both statistic in each square subfield individually, and then take the average over all subfields for further estimation. The 2PCFs and the power spectra are both computed over a finite range of angular scales. We chose the minimum scale to be 1 arcmin ($\ell = 21,600$) based on a map pixel size of ~ 0.4 arcmin. Considering that the linear angular size of each square field is ~ 200 arcmin, we chose the maximum scale to be 60 arcmin ($\ell = 360$), which is consistent with L15.

In addition to the average value of both statistic, we make use of 1000 realizations of each cosmological model to calculate their variance. Hereafter, we use $\xi_{\pm}(\theta)$ and $P(\ell)$ to represent 2PCFs and power spectra, and use $\sigma_{\xi_{\pm}}$ and σ_P to represent the uncertainty of the mean values in terms of their standard deviation.

3.1.1 Two-point correlation function

Following Schneider et al. (2002), the two components $\xi_{+}(\theta)$ and $\xi_{-}(\theta)$ of the 2PCF of the lensing shear field are estimated by

$$\xi_{\pm}(\theta) = \frac{\sum_{ij} w_i w_j [e_t(\boldsymbol{\theta}_i) e_t(\boldsymbol{\theta}_j) \pm e_{\times}(\boldsymbol{\theta}_i) e_{\times}(\boldsymbol{\theta}_j)]}{\sum_{ij} w_i w_j} \quad (12)$$

where $\theta = |\boldsymbol{\theta}_i - \boldsymbol{\theta}_j|$ is the angular scale, and e_t, e_{\times} the tangential and cross components of the galaxy ellipticity. The

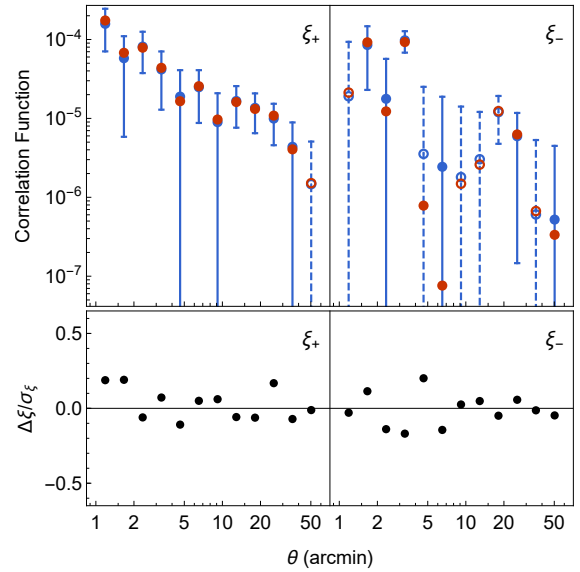


Figure 2. The upper panel shows 2PCFs calculated by the brute-force method (red) and our faster grid-based method (blue). The error bars show the 68% confidence interval of the correlation between ellipticities in each bin. Negative values are shown as empty circles/dashed error bars. The lower panel shows the residuals in units of the standard deviation. The calculations are performed on the ellipticities of the galaxies in the first subfield (RA $35.3^{\circ} \sim 38.8^{\circ}$, Dec $-11.3^{\circ} \sim -7.8^{\circ}$).

summation over all pairs of galaxies are performed within θ -bins evenly spaced on a logarithmic scale, with the low- θ boundary of the i -th bin given by $\theta_i = 1.41^i$ arcmin, where $i = 0, 1, 2, \dots, 11$.

There are between 200 – 400 thousand galaxies in each subfield, making a summation over every pair of galaxies computationally challenging. We wrote our own implementation of a code to calculate the correlation function using a grid-based method, where we gradually decrease the size of the cells to maintain accuracy at smaller and smaller angular scale. The idea is similar to *Athena* (see § 5 in Schneider et al. 2002). The primary limitation of using a grid-based method is that the angular resolution is lower. Our method is implemented so that the minimum resolution is $\Delta\theta/\theta = 0.05$ at $\theta = 1$ arcmin and the maximum resolution is $\Delta\theta/\theta = 0.01$ for $\theta \gtrsim 5$ arcmin. As a reference, the resolution used by Kilbinger et al. (2013) was $\Delta\theta/\theta = 0.03$ for all scales.

Figure 2 shows the result of our method compared to the brute-force method. While there are residuals, they are relatively small $\Delta\xi/\sigma_{\xi} \lesssim 0.3$. Furthermore, we perform the calculations on the real and the mock shear catalogues in the same way, with only the numerical values of the ellipticities being different. Therefore, we do not expect a bias in our parameter estimation, in spite of the existence of the small residuals.

3.1.2 Power spectrum

We perform an FFT of each convergence field on a 512×512 grid and compute the power spectra in 38 logarithmic multipole bins over the range $360 < \ell < 21,600$, where the

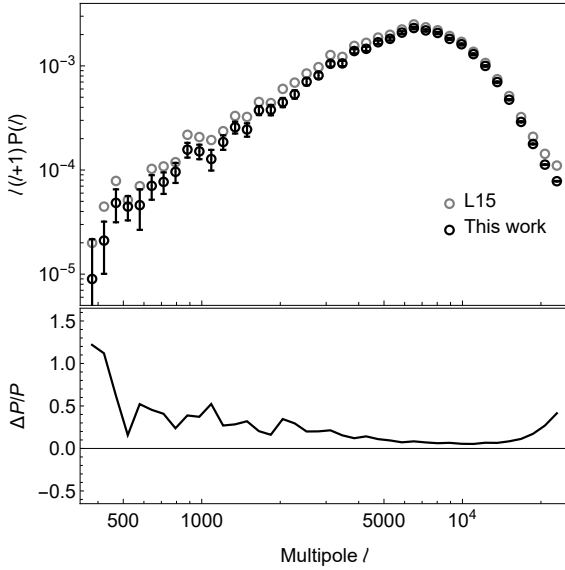


Figure 3. The upper panel shows the power spectrum (with error bars corresponding to a standard deviation in each bin) calculated in this work, and that by L15’s method, on the first subfield. The lower panel shows the relative differences between the two.

low- ℓ boundary of the i -th multipole bin is $\ell_i = 60^{i/38} \times 360$, where $i = 0, 1, 2, \dots, 37$.

In Figure 3, we compare the power spectrum we derive from a subfield with that obtained by L15’s method. L15 pointed out two artefacts in their power spectra: (1) the finite pixel size causes extra power at $\ell \gtrsim 20,000$, and (2) hard cut-offs at the edges of the masks, i.e. low number density regions, cause extra power at $\ell \gtrsim 7,000$. Compared to L15, we obtain a lower power over all scales because we remove the second artefact by considering the contribution of low-density regions.

3.2 Parameter estimation

We estimate the posterior probability distribution in the parameter space $\mathbf{p} \in \{\Omega_m, \sigma_8\}$ in a standard way, using Bayes’ theorem. Assuming a model M and the observed data \mathbf{d} , the posterior distribution is

$$p(\mathbf{p}|\mathbf{d}, M) = \frac{p(\mathbf{d}|\mathbf{p}, M) p(\mathbf{p}|M)}{p(\mathbf{d}|M)}. \quad (13)$$

We adopt uniform distributions on $0.1 \leq \Omega_m \leq 0.8$ and $0.1 \leq \sigma_8 \leq 1.4$ for the prior $p(\mathbf{p}|M)$, and the likelihood function is given by

$$\log p(\mathbf{d}|\mathbf{p}, M) \propto -[\mathbf{d} - \mathbf{y}(\mathbf{p})]^T \mathbf{C}^{-1}(\mathbf{p}) [\mathbf{d} - \mathbf{y}(\mathbf{p})], \quad (14)$$

where $\mathbf{y}(\mathbf{p})$ are the values of observables from the N -body simulation and \mathbf{C} the covariance matrix. Here, we assume the statistics follow multivariate Gaussian distributions. In general, $\mathbf{C} = \mathbf{C}(\mathbf{p})$ is a function of cosmological model, but a constant covariance is often used in the literature since it gives reasonable estimates. We use cosmology-dependent covariances to obtain our primary results, and then compare these with results using constant covariances in § 5.2.

Finally, we need to interpolate from the 91 discrete cosmological models to obtain the continuous function $\mathbf{y}(\mathbf{p})$. For

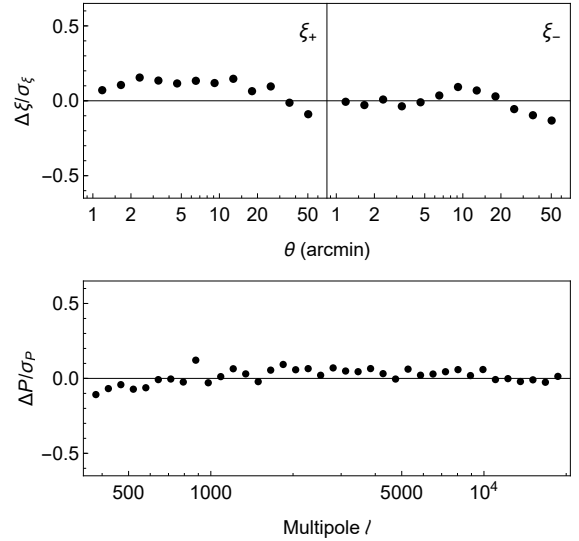


Figure 4. The residuals between the interpolated 2PCFs and the power spectrum, relative to their true (directly measured) values. The residuals are divided by the corresponding standard deviation in each bin. The statistics are averaged over all 13 subfields.

each of the 91 simulated models, we measure 2PCFs and power spectra for all realizations, and find their averages over all realizations, together with their covariances. Then, we interpolate between these models to obtain the mean statistics and the covariances in the 3D parameter space using polynomial fitting. Note that the mean statistics and covariances are highly correlated among cosmological models, so we can reduce their dimensions using principal component analysis (PCA; Wold et al. 1987) to avoid over-fitting.

After some experimentation and testing, we found the best performance by setting the number of principal components $N_{\text{PC}} = 5$ and fitting using polynomials up to 5th order. To illustrate the accuracy, we pick a fiducial model ($\Omega_m = 0.305$, $\sigma_8 = 0.765$, $w = -0.879$) closest to the Planck 2018 values, remove it from the polynomial fitting dataset, and compare the predicted values with the true values. As shown in Figure 4, the residuals are below 0.2σ , i.e. much smaller than the uncertainty for both statistics, giving us confidence that the interpolation errors will not significantly affect parameter estimation. Note that we interpolate along the direction of w , but our analysis in this paper is restricted to the hyperplane $w = -1$, corresponding to Λ CDM.

4 RESULTS

4.1 Inferences from the 2PCF vs. the power spectrum

We first reproduce the discrepancy between Kilbinger et al. (2013) and L15 introduced only by the difference in methods, where the shear catalogues, N -body simulation, and data processing are exactly the same.

Figure 5 shows confidence contours enclosing 68% and 95% of the likelihood from the power spectrum and from the 2PCF. The parameter combination $\sigma_8(\Omega_m/0.27)^\alpha$ (marginalised over the orthogonal direction in $[\sigma_8, \Omega_m]$ parameter space) is best constrained with $\alpha = 0.64$ for the

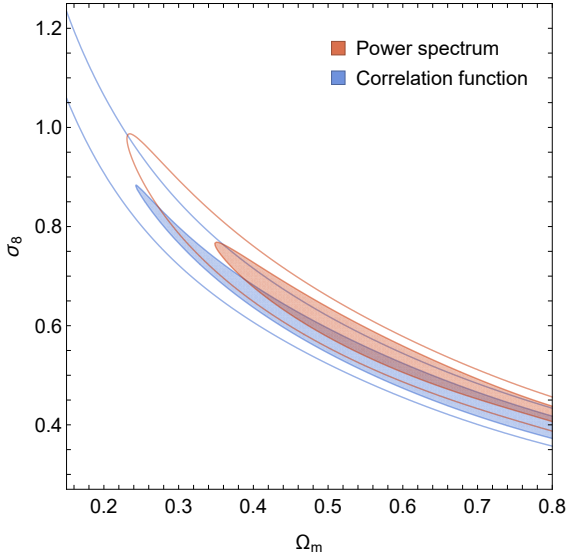


Figure 5. 68% and 95% joint confidence contours on σ_8 and Ω_m , using the power spectrum and the 2PCF, as labelled. The power spectrum yields an $\sim 8\%$ larger normalization, comparable to the $\sim 10\%$ difference between L15 and Kilbinger et al. (2013).

2PCF and $\alpha = 0.66$ for the power spectrum. We use a fixed $\alpha = 0.65$ for simplicity, and we use $\Sigma_8 \equiv \sigma_8(\Omega_m/0.27)^{0.65}$ in order to do direct comparisons.

The best fits we find are $\Sigma_8 = 0.833 \pm 0.035$ using the 2PCF, and $\Sigma_8 = 0.896 \pm 0.038$ using the power spectrum. Compared to the $\sim 10\%$ discrepancy on Σ_8 between Kilbinger et al. (2013) and L15, we find a comparable $\sim 8\%$ difference, which is attributable entirely to the use of a different statistic.

4.2 Systematic biases

In this section, we test whether there may be a systematic bias in parameter estimates derived through either statistic. To do this, we constrain the cosmological parameters of a fiducial model from the mock catalogues – that is, we fit our own simulations, rather than the observational data. In each of the 1000 realizations of the fiducial model ($\Omega_m = 0.305$, $\sigma_8 = 0.765$, $w = -0.879$) we create a mock shear catalogue, and treat it as the real catalogue to derive probability distributions in the Ω_m - σ_8 space, and to compute the corresponding constraint on Σ_8 .

Figure 6 shows the distribution of the 1000 best-fit $\sigma_8(\Omega_m/0.27)^\alpha$ ($\alpha = 0.65$) values, using both the 2PCF and the power spectrum. The true value in the fiducial model is $\Sigma_8 = 0.828$, whereas the 2PCF and the power spectrum yield average values of $\Sigma_8 = 0.800 \pm 0.001$ and $\Sigma_8 = 0.793 \pm 0.001$, respectively. The difference between these values estimated from the two methods is $\delta\Sigma_8 = 0.007$, which is nearly an order of magnitude smaller than required to explain the difference ($\delta\Sigma_8 = 0.896 - 0.833 = 0.063$) found in § 4.1 above.

On the other hand, we observe a systematic bias, with both statistics under-predicting the true value by $\delta\Sigma_8 = -0.03$. There are two primary reasons for such a bias. First, the usage of $\Sigma_8 = \sigma_8(\Omega_m/0.27)^\alpha$ as a parameter assumes a power-law form for the degeneracy between Ω_m and σ_8 . But the probability distributions deviate from a power-law,

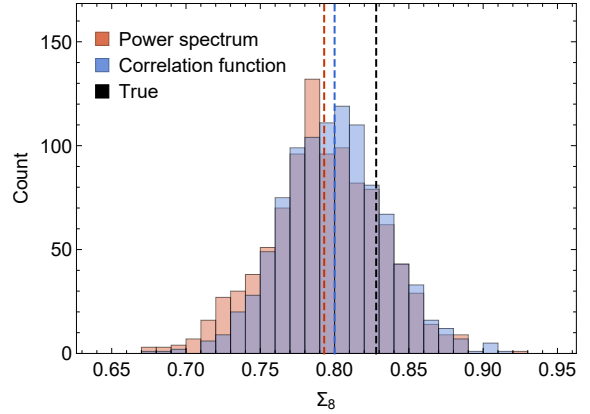


Figure 6. We fit the 2PCF and the power spectrum to simulated, rather than real observed data, to check for systematic biases. The figure shows the distribution of $\Sigma_8 \equiv \sigma_8(\Omega_m/0.27)^{0.65}$ inferred from 1000 realizations of mock shear catalogues in the fiducial cosmological model, using the two statistics. A cosmology-dependent covariance matrix is used. The average values are shown by the dashed vertical lines, and the true value is marked for comparison. Both statistics are biased low, by nearly the same amount.

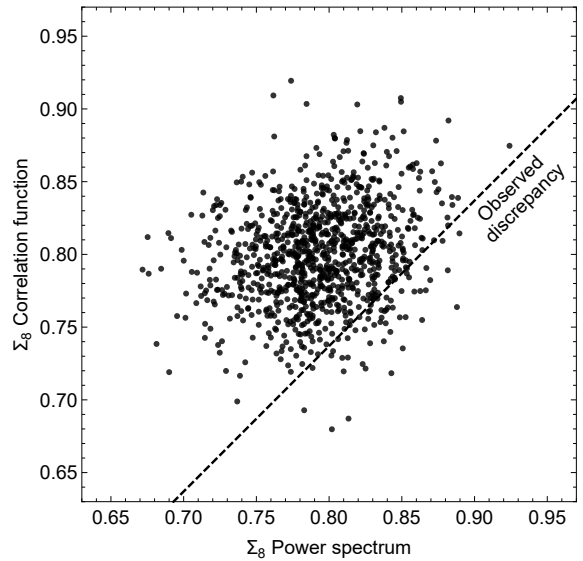


Figure 7. The scatter plot of the Σ_8 values estimated from the 2PCF and the power spectrum in each of the individual 1000 realizations of the fiducial model. The discrepancy arising when fitting the CFHTLenS data (§ 4.1) is shown by the dashed line. A discrepancy as large as the observed one is reproduced by chance in only $53/1000=5.3\%$ of the realizations.

regardless of the statistic (Hikage et al. 2019; Lin & Kilbinger 2015), causing the maximum-likelihood estimators to be biased (Lin & Kilbinger 2015). Second, a model with cosmology-dependent covariance is known to give a slightly lower Σ_8 estimate compared to the true value (Eifler et al. 2009), because it gives more weights to low- Σ_8 cosmological models.

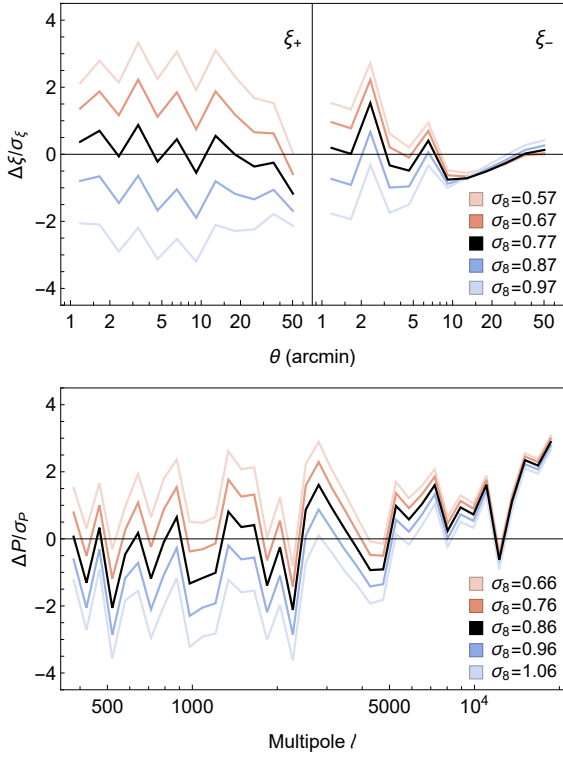


Figure 8. The differences in the 2PCFs and the power spectra, in units of their standard deviations, between the CFHTLenS data and in ray-tracing simulations in a range of cosmologies. We use a fixed $\Omega_m = 0.3$ and a range of σ_8 values as shown in the legends. The best fits for σ_8 are shown in black.

4.3 Statistical fluke

The possibility that the discrepancy is caused simply by a statistical fluke should also be considered. We test the probability of this by measuring the fraction of realizations of the mock shear catalogues which yield a discrepancy equal to or larger than the observed one. Figure 7 shows a scatter plot of Σ_8 inferred from the two statistics in the 1000 individual realizations. The correlations are visibly weak (with a correlation coefficient of $R = 0.22$). By counting the number of points with $\Delta\Sigma_8 \geq 0.063$, we find that the chance of the observed discrepancy among the realizations due to randomness is 5.3%. Therefore, we conclude that a statistical fluke is not a particularly compelling explanation: its likelihood is the same as the significance of the original discrepancy (both at the $\approx 2\sigma$ level).

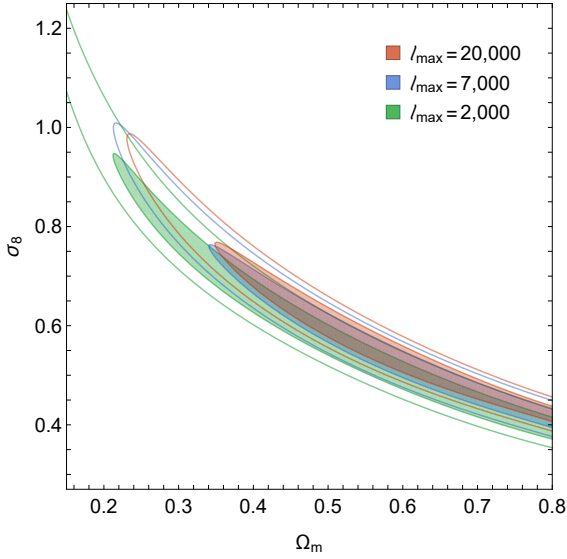


Figure 9. 68% and 95% joint confidence contours on σ_8 and Ω_m , using the power spectrum with different multipole cut-offs. $\ell_{\max} = 20,000$ was used for our results in § 4.1, whereas the more conservative cut-offs at $\ell_{\max} = 7,000$ and $\ell_{\max} = 2,000$ were used by L15 and by Hikage et al. (2019), respectively. Excising small scales reduces the best-fits σ_8 values; $\ell_{\max} = 2,000$ brings the results from the power spectrum in agreement with the 2PCF.

Table 1. Constraints on Σ_8 from different statistics.

Method	ℓ_{\max}	Σ_8	α
Power spectrum	20,000	0.896 ± 0.038	0.65
	7,000	0.877 ± 0.038	
	2,000	0.836 ± 0.044	
Correlation function	—	0.833 ± 0.035	

4.4 Shapes of 2PCFs and power spectra

Finally, we check the profiles of the 2PCFs and the power spectra in the real data, against those derived from N -body simulations. The differences between the two are shown as a function of angular scale in Figure 8. From the spreads and biases of the residuals seen in this figure, we find that the 2PCF and the power spectrum constrain σ_8 on different scales. For the 2PCF, values from all scales of ξ_+ are similarly constraining, while for ξ_- , smaller scales ($\lesssim 5$ arcmin) are much more important. For the power spectrum, the situation is the reverse: most of the constraints come from relatively large scales ($\ell \lesssim 4000$, corresponding to $\gtrsim 5$ arcmin).

A conspicuous feature in Figure 8 is that the real data has excess power on small scales ($5,000 \lesssim \ell \lesssim 20,000$), compared to the simulations, by $\sim (1-3)\sigma$. Such an excess power reveals the fact that the real data differs from what can be generated by the N -body simulations. More interestingly, this excess small-scale difference only occurs in the power spectra, without affecting 2PCFs, even though the two statistics are covering the same range of angular scales (1–60 arcmin).

In order to investigate the impact of this excess power on the parameter estimates, we repeated our analysis with a more conservative choice of multipole cut-offs. In Figure 9, we show the results from three multipole variations: (i) $\ell_{\max} = 20,000$ (our original choice), (ii) $\ell_{\max} = 7,000$ (used by L15 to avoid various artefacts on small scales); and (iii) $\ell_{\max} = 2,000$ (similar to the value used by Hikage et al. 2019

Table 2. Constraints on Σ_8 from different statistics, but including all fields (including those failing a systematics test).

Method	ℓ_{\max}	Σ_8	α
Power spectrum	20,000	0.883 ± 0.034	0.65
	7,000	0.860 ± 0.034	
	2,000	0.818 ± 0.040	
Correlation function	—	0.853 ± 0.036	

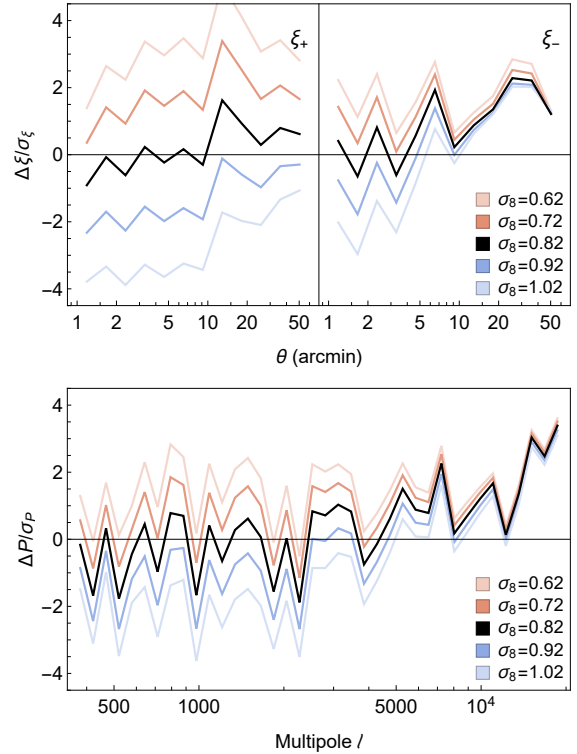


Figure 10. The same as Figure 8, except the systematics test selection is not applied to the data (i.e. all fields are included). Note that the best fit value for σ_8 (black) is different from Figure 8.

to avoid the impact of the one-halo term). The corresponding marginalised constraints on Σ_8 are shown in Table 1. We find that a power spectrum cut-off at lower ℓ_{\max} decreases the inferred Σ_8 values, and the power spectrum yields results consistent with the 2PCF for $\ell_{\max} = 2,000$. This demonstrates that the excess power on small scales in the power spectrum explains the discrepancy with 2PCF.

5 DISCUSSION

5.1 Field selection

As mentioned in § 2.1, 25% of the CFHTLenS data have been found to fail a systematics test. In this section, we repeat our previous analysis (§ 4), which was based on the 75% of the fields passing the systematics test, but this time we retain the failed fields.

Table 2 shows the marginalised constraints on Σ_8 using all CFHTLenS data, and Figure 10 shows the comparison between the resulting 2PCFs and power spectra in the real data and those from the mock catalogues. We find that the excess power in the power spectrum exists regardless

Table 3. Constraints on Σ_8 from different statistics, but with a constant (cosmology-independent) covariance matrix.

Method	ℓ_{\max}	Σ_8	α
Power spectrum	20,000	0.911 ± 0.038	0.65
	7,000	0.890 ± 0.040	
	2,000	0.847 ± 0.047	
Correlation function	—	0.847 ± 0.042	

of the systematics test selection. We also find that the inclusion of the data failing the systematics test significantly alters 2PCFs, leading to excess correlations on large scales at $1\sigma \sim 2\sigma$ level for ξ_+ and ξ_- . This is consistent with the reason these fields were excluded by the CFHT team (Heymans et al. 2012). Note that these systematic errors would drive estimates of Σ_8 from the 2PCF higher. Overall, we find no evidence that residual systematics would help explain the observed difference between the 2PCF and the power spectrum.

5.2 Cosmology-dependent vs. constant covariance

The results of using a constant covariance matrix are shown in Table 3. We find that the inferred Σ_8 values are uniformly higher than those in the cosmology-dependent covariance case, by $\Delta\Sigma_8 \approx 0.014$ in each case. The constant covariance model underestimates the uncertainty of the statistics in the cosmological models with low Ω_m and/or σ_8 and overestimates them for high Ω_m and/or σ_8 . Therefore, in the case of constraining a marginalised parameter Σ_8 , the constant covariance model has the tendency to overestimate the likelihood of high Σ_8 , yielding higher best-fit values.

Despite this overall shift to higher values, the differences between the values of Σ_8 between the 2PCF and the power spectrum remain similar. Therefore, we conclude that the assumed cosmology-dependence of the covariance matrix does not explain the apparent discrepancy.

5.3 Reconstruction of the shape noise

The power spectra that we measured from the CFHTLenS Catalogue and the mock catalogues consist of the lensing signal from the large-scale structures, plus the random shape noise. Based on the fiducial cosmological model, we find in Figure 11 that the lensing signal power P_{signal} accounts for $\sim 25\%$ of the total power at $\ell = 400$, but merely $\sim 0.1\%$ at $\ell = 20,000$. Because the shape noise power P_{noise} dominates the total power, the accuracy of shape noise reconstruction is very important on small scales. Here, we discuss two inaccuracies in shape noise reconstruction as follows.

5.3.1 Shape noise contamination

We use randomly rotated ellipticities from the CFHTLenS Catalogue as our proxy for the shape noise in the mock catalogues. An inaccuracy from this method is that the true lensing shear in the data is included as part of the shape noise. As a result, the shape noise power in the mock catalogues is contaminated and overestimated. We find that the dispersion of the lensing shear in the noiseless mock catalogues is

$$\langle |e_{\text{signal}}|^2 \rangle = 2 \times 10^{-4}, \quad (15)$$

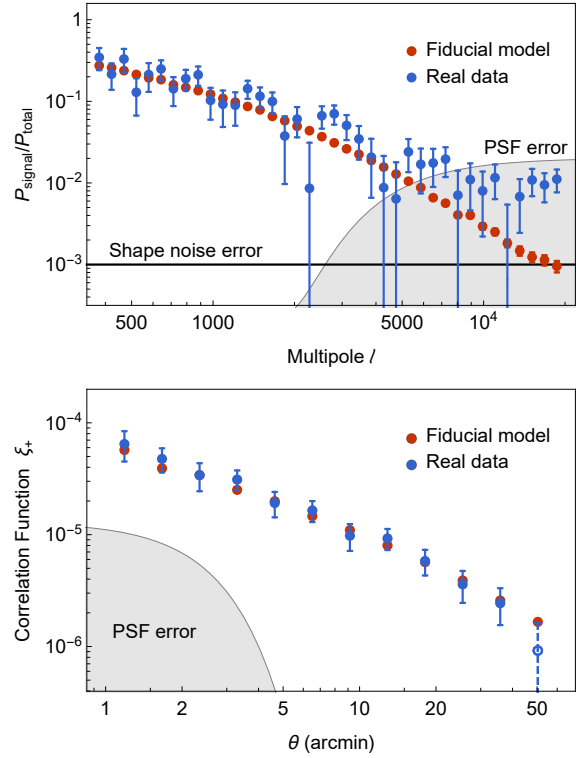


Figure 11. The upper panel shows the contribution of the lensing signal to the total (=signal+noise) power spectrum in the fiducial model (red). For comparison, we also show the difference between the power measured in the real data and the expected noise (blue; assuming the same shape noise power, and again divided by the same total power). The excess power shown in Figure 8 also appears here at $\ell > 5,000$. The estimated error in the shape noise is shown by the horizontal black line. The grey shaded region shows the possible range of residual power from PSF modelling errors (see § 5.3.2). The lower panel shows the residual correlation from PSF modelling errors compared with the 2PCF ξ_+ (note that the shape noise is assumed to be uncorrelated and not to contribute).

while the dispersion of the observed galaxy ellipticities is

$$\langle |e_{\text{total}}|^2 \rangle = 2 \times 10^{-1}. \quad (16)$$

Note that the random rotations erase the correlations in the signal contribution to the measured ellipticities, so that our adopted shape noise power is overestimated by a constant, scale-independent factor of

$$\delta P/P_{\text{total}} = \langle |e_{\text{signal}}|^2 \rangle / \langle |e_{\text{total}}|^2 \rangle = 10^{-3}, \quad (17)$$

as is shown in Figure 11. Comparing the shape noise error to the power spectrum of the lensing signal in the real data, we find it to be subdominant across all scales.

5.3.2 Point spread function residual correlation

Point spread function (PSF) modelling also introduces inaccuracies to the shape noise reconstruction. According to the CFHTLenS pipeline (Erben et al. 2013), PSFs at the locations of galaxies are estimated based on nearby star images on the chip level, where a two-dimensional second-order polynomial is used to model the local PSF anisotropy. Then, the influence of PSF anisotropy is removed from the

galaxies. The PSF estimation method adopted in producing the CFHTLenS Catalogue was global third-order polynomials with some coefficients varying between CCDs (Miller et al. 2013). The impact of PSF residual correlations for CFHTLenS was studied by Lu et al. (2017). While the above method was not specifically investigated, a similar method – second-order polynomial fits on CCDs – has been shown in Lu et al. (2017) to produce residual correlations in lensing shear field of $3 \times 10^{-6} \lesssim \delta\xi_+ \lesssim 10^{-5}$ between $1 \text{ arcmin} < \vartheta < 3 \text{ arcmin}$, which can be taken as an upper limit.

This residual correlation is subdominant to the shear-shear correlation function (with a $\sim 10\%$ contribution on small scales; see the bottom panel of Figure 11). Nevertheless, we find that it can have a non-negligible impact on inferences from the power spectrum. The Wiener-Khinchin theorem (Wiener 1930) states that the correlation function and the power spectrum are related through a Fourier transform. Using this relation, we calculate the estimated error in the power spectrum by adding artificial noise to the mock catalogues according to the PSF residual correlation. In Figure 11, we show the possible range of PSF error assuming the residual correlation given by Lu et al. (2017) as an upper limit. The PSF error is again subdominant to the total power, representing a $\sim 1\%$ contribution on small scales ($\ell \gtrsim 4,000$). However, unlike for the 2PCF, this exceeds the expected contribution of the large-scale structure signal on these scales, and it is also comparable to the excess power seen in the real data ($\delta P/P_{\text{total}} \sim 10^{-2}$). Therefore, we consider the PSF residual correlation to be a possible explanation for the excess power. As discussed above (see Fig. 8), the power-spectrum constraints are driven by somewhat larger scales, but the excess small-scale power is still a plausible reason for driving up the inferred Σ_8 value.

5.4 Choice of spectral index in N -body simulations

We next explore the possibility that the choice of the spectral index n_s may explain the excess power on small scales. In the N -body simulations, we use a pre-defined set of cosmological parameters (see § 2.3) based on WMAP (Komatsu et al. 2011). Our choice of $n_s = 0.96$ is lower than the more recent and more accurate value $n_s = 0.965 \pm 0.004$ from Planck 2018 (TT,TE,EE+lowE+lensing) by up to $\sim 1\%$. With the fluctuation amplitude anchored at $8h^{-1} \text{ Mpc}$ by σ_8 , n_s changes the logarithmic slope of the power spectrum around this pivot scale. We now quantitatively study its impact on the lensing signal power spectrum.

The CFHTLenS galaxy catalogue shows a median redshift of ~ 0.7 , corresponding to an angular scale of 400 kpc/arcmin . In this case, the simulations correctly reconstruct the desired density fluctuation at 30 arcmin or equivalently $\ell = 800$. We expect the N -body simulations to underestimate the power spectra on smaller scales ($\ell > 800$). In terms of P_{signal} , for each percent of increase in n_s , the power would be increased by 1.8% at $\ell = 5,000$ and 3.3% at $\ell = 20,000$. However, we find that the lensing signal power in the real data is higher than in the fiducial model by a factor of order unity or more at $\ell > 5,000$ (see Figure 11). This is much greater than could be attributed to our choosing an incorrect n_s . We therefore rule out this possibility.

5.5 Intrinsic alignment

We also consider intrinsic alignment as an explanation for the excess small-scale power. Intrinsic alignment describes the phenomenon in which ellipticities of galaxies are correlated not only through gravitational lensing but also in real space, through the physics of galaxy formation. It is a well-known contamination to weak lensing measurements. King & Schneider (2003) and Heymans et al. (2004) have found that modelling intrinsic alignment is crucial for tomographic weak lensing measurements using multiple redshift bins. Although a two-dimensional analysis, as in this work, is less affected. Schneider & Bridle (2010) and Sifón et al. (2015) have found intrinsic alignment to alter the profile of 2D lensing power spectra significantly on small scales, for a fiducial medium-deep survey.

According to the theoretical estimates by Sifón et al. (2015), a nonlinear alignment model would cause a 50% increase in P_{signal} on the scale of $\ell = 10,000$. Comparing this value to the observed discrepancy of a factor of ≈ 3 at $\ell = 10,000$ in Figure 11, we find that intrinsic alignment is able to explain only $\sim 20\%$ of the excess power.

5.6 Baryonic effects

We finally briefly consider baryonic effects as a possible reason for the excess power. The impact of baryon physics on the power spectrum and correlation function, under different assumptions about star-formation and feedback, has been investigated by several authors. In particular, Semboloni et al. (2011, 2013) and Chisari et al. (2018) compared the power spectrum and the 2PCF from a dark-matter-only reference simulation to these quantities in simulations that include the cooling and condensation of baryons in DM halos, as well as star formation and AGN feedback that drives gas out of halos. In general, they found that cooling enhances power on the smallest scales, but on the scales of interest here, corresponding to $\ell < 20,000$, or $k \lesssim 3h \text{ Mpc}^{-1}$, the baryon effects (especially when AGN feedback is included) suppress both the power spectrum and the 2PCF ξ_+ by $\sim 1 - 10\%$. This difference is below the uncertainty of the power spectrum measurements, and has the opposite sign. We conclude that baryonic effects are unlikely to explain the excess power on arcmin scales.

6 CONCLUSION

Based on the same data from CFHTLenS, Kilbinger et al. (2013) and Liu et al. (2015) derived constraints on Σ_8 that differ by 10% ($\sim 2\sigma$). We investigated this difference, motivated by the fact that the lower value (Kilbinger et al. 2013) is in tension, while the higher value (Liu et al. 2015) is in agreement with the CMB corresponding constraints from the CMB. We find that this discrepancy originates from the difference in the statistics used in the two studies: the 2PCF of the shear vs. the power spectrum of the convergence. We have done a fair comparison of these two statistics and reproduced a similar discrepancy ($\sim 8\%$). The discrepancy exists regardless of whether we adopt a cosmology-dependent or constant covariance matrices in our analysis.

By examining the scale-dependence of the 2PCF and

the power spectrum, we find that the power in the real data in the range $5,000 < \ell < 20,000$ is significantly larger than in the N -body simulations used to fit the data. We identify this excess small-scale power as the main reason that the power spectrum yields an unusually high Σ_8 (i.e. higher than in other WL studies). We find that this excess power exists regardless of whether CFHTLenS fields that fail a systematics test are included or not. When we chose a lower cut-off $\ell_{\max} = 2,000$ for the power spectrum, we recovered agreement between the Σ_8 values inferred from the power spectrum and the 2PCF. This demonstrates that the small-scale excess power is the reason for the discrepant Σ_8 values.

We speculate that two possible effects explain the excess power. First, we find that PSF residual correlations may have introduced an error in the power spectrum, causing an overestimate by up to $\sim 10^{-2} P_{\text{total}}$. This is comparable to the excess power seen in the real data at $\ell > 4,000$, and thus a possible explanation for this excess. Second, intrinsic alignment of galaxies is expected to increase the amplitude of the lensing power spectrum by $\sim 50\%$, which could explain up to $\sim 20\%$ of the excess power. In addition, we find that baryonic effects are expected to be too small and in the wrong direction to cause the excess power.

Overall, we conclude that the value of σ_8 found recently by Liu et al. (2015), which is $\sim 10\%$ higher than in other lensing analyses and is in agreement with the corresponding CMB constraints, is due to the excess small-scale power in the CFHTLenS data, which affects the power spectrum (but not the 2PCF). This excess is likely a residual artefact, and therefore it does not resolve the tension between the matter density fluctuation amplitudes measured in lensing and in the CMB data. A more general lesson from our results is that analysing the 2PCF and the power spectrum in tandem could be a useful tool to discover (and to help control) systematic errors.

ACKNOWLEDGEMENTS

We thank Greg Bryan, Martin Kilbinger and Jerry Ostriker for useful discussions, and acknowledge support from NASA ATP grant 80NSSC18K1093.

REFERENCES

- Abbott T., et al., 2016, Monthly Notices of the Royal Astronomical Society, 460, 1270
- Ade P. A., et al., 2016, Astronomy & Astrophysics, 594, A13
- Aghanim N., et al., 2018, arXiv preprint arXiv:1807.06209
- Aihara H., et al., 2017a, Publications of the Astronomical Society of Japan, 70, S4
- Aihara H., et al., 2017b, Publications of the Astronomical Society of Japan, 70, S8
- Bartelmann M., Schneider P., 2001, Physics Reports, 340, 291
- Benitez N., 2000, The Astrophysical Journal, 536, 571
- Bertin E., Arnouts S., 1996, Astronomy and Astrophysics Supplement Series, 117, 393
- Chisari N. E., et al., 2018, Monthly Notices of the Royal Astronomical Society, 480, 3962
- Eifler T., Schneider P., Hartlap J., 2009, Astronomy & Astrophysics, 502, 721
- Erben T., et al., 2013, Monthly Notices of the Royal Astronomical Society, 433, 2545
- Heymans C., Brown M., Heavens A., Meisenheimer K., Taylor A., Wolf C., 2004, Monthly Notices of the Royal Astronomical Society, 347, 895
- Heymans C., et al., 2012, Monthly Notices of the Royal Astronomical Society, 427, 146
- Hikage C., et al., 2019, Publications of the Astronomical Society of Japan, 71, 43
- Hildebrandt H., et al., 2016, Monthly Notices of the Royal Astronomical Society, 465, 1454
- Hoekstra H., Jain B., 2008, Annual Review of Nuclear and Particle Science, 58, 99
- Kaiser N., Squires G., 1993, The Astrophysical Journal, 404, 441
- Kilbinger M., 2015, Reports on Progress in Physics, 78, 086901
- Kilbinger M., et al., 2013, Monthly Notices of the Royal Astronomical Society, 430, 2200
- King L. J., Schneider P., 2003, Astronomy & Astrophysics, 398, 23
- Köhlinger F., et al., 2017, Monthly Notices of the Royal Astronomical Society, 471, 4412
- Komatsu E., et al., 2011, The Astrophysical Journal Supplement Series, 192, 18
- Kuijken K., et al., 2015, Monthly Notices of the Royal Astronomical Society, 454, 3500
- Lin C.-A., Kilbinger M., 2015, Astronomy & Astrophysics, 576, A24
- Liu J., Haiman Z., Hui L., Kratochvil J. M., May M., 2014, Physical Review D, 89, 023515
- Liu J., Petri A., Haiman Z., Hui L., Kratochvil J. M., May M., 2015, Physical Review D, 91, 063507
- Lu T., Zhang J., Dong F., Li Y., Liu D., Fu L., Li G., Fan Z., 2017, The Astronomical Journal, 153, 197
- McKay M. D., Beckman R. J., Conover W. J., 1979, Technometrics, 21, 239
- Miller L., et al., 2013, Monthly Notices of the Royal Astronomical Society, 429, 2858
- Refregier A., 2003, Annual Review of Astronomy and Astrophysics, 41, 645
- Schneider M. D., Bridle S., 2010, Monthly Notices of the Royal Astronomical Society, 402, 2127
- Schneider P., van Waerbeke L., Kilbinger M., Mellier Y., 2002, Astronomy & Astrophysics, 396, 1
- Semoloni E., Hoekstra H., Schaye J., van Daalen M. P., McCarthy I. G., 2011, MNRAS, 417, 2020
- Semoloni E., Hoekstra H., Schaye J., 2013, MNRAS, 434, 148
- Sifón C., Hoekstra H., Cacciato M., Viola M., Köhlinger F., van der Burg R. F., Sand D. J., Graham M. L., 2015, Astronomy & Astrophysics, 575, A48
- Springel V., 2005, Monthly notices of the royal astronomical society, 364, 1105
- Troxel M. A., et al., 2018, Physical Review D, 98, 043528
- Wiener N., 1930, Acta Mathematica, 55, 117
- Wold S., Esbensen K., Geladi P., 1987, Chemometrics and Intelligent Laboratory Systems, 2, 37